Simulations of the collection of mesospheric dust particles with rocket instrument

Adrien Pineau[1], Henriette Trollvik[2,3], Sveinung Olsen[2], Yngve Eilertsen[2], and Ingrid Mann[2]

[1]Laboratory for Laser Energetics, University of Rochester, 250 E. River Rd, Rochester, New York, USA
[2]Department of Physics of Technology, UiT Artic University of Norway, 9037 Tromsø, Norway
[3]Space and Plasma Physics - KTH Royal Institute of Technology, Teknikringen 31, 10044 Stockholm, Sweden

Correspondence: Ingrid Mann (ingrid.b.mann@uit.no)

Abstract. We investigate the collection of dust from the mesosphere with the MESS instrument that is designed to fly on a sounding rocket. The instrument consists of a collection device with an opening and closure mechanism and an attached conic funnel. Attaching the funnel increases the sampling area in comparison to the collection area. The instrument will collect primary particles that directly hit the collection area and secondary particles that form from mesospheric dust hitting the funnel.
5 We simulate the entry and impact of dust onto the detector considering their trajectories in the airflow and the fragmentation at the funnel. We estimate the collection efficiency of the instrument and the impact energy of particles at the collecting area. The design considered has a sampling area of 5 cm diameter and a collection area of 1.8 cm diameter.

We use the results of the calculations to estimate the amount of dust that MESS (MEteoric Smoke Sampler) can collect during a rocket flight. We consider meteoric smoke particles (MSP) based on a model of the MSP distribution. In addition we assume
10 that water ice particles that form close to the mesopause contain a fraction of smaller MSP. The water ice sublimates during the collection or later during rocket flight so that only refactory material remains. Assuming the collected particles contain 3% volume fraction of MSP, we find that the instrument would collect of the order of 10^{14} to 10^{15} amu of refractory MSP particles. The estimate basis on the assumption that the ice components are melting and the flow conditions in the instruments are for typical atmospheric pressures at 85 km. Aside from the instrument conditions that we investigate in this paper, our estimate
15 of the mass that we expect to collect with MESS applies the results from a particle transport model for the meteoric smoke particles and from the description of noctilucent cloud particles based on published model and observational results.

1 Introduction

The upper atmosphere at the lower layer of the ionosphere contains small solid dust particles and under certain conditions ice particles. Dust particles, referring hereby to both refractory and ice particles, take part in chemical processes (Plane et al., 2015).
The ice particles notably cause mesospheric phenomena such as the Noctilucent Clouds (NLC) and the Polar Mesospheric Summer Echoes (PMSE) observed with radar (Rapp and Lübken, 2004). The solid refractory particles, denoted as Meteoric Smoke Particles (MSP) originate from cosmic dust material that remains in the upper atmosphere as a result of the meteor process. During their entry in the upper Earth's atmosphere, meteors are heated and ablated when they reach altitudes between 120 km and 80 km above the Earth's surface (e.g., Mann, 2009). These remnants of the cosmic dust condense into nm-sized particles. The conditions for the direct formation of ice particles from the gas by homogeneous condensation are unfavorable (e.g., Tanaka et al., 2022) and MSP are a possible candidate to facilitate heterogeneous nucleation. This formation process happens during summer months at mid and high latitudes as it corresponds to when and where the mesopause temperature is sufficiently low for ice formation. PMSE are strong coherent structures in the electron number density observed by VHF radars, that occur due to the presence of small ice particles,, i.e. with a radius smaller than ~ 20nm, which the typical wavelengths of the scattered radars range from 1m to 10m. They are observed at altitudes from 80 to 90 km with a peak around 85km and evidence the presence of ice particles. NLC are associated to the cloudy patterns that can be seen directly from the Earth's surface during the twilight when the sun light is reflected because of large ice particles, i.e. those with radii larger than ~ 20 nm. They are observed between 80 km and 85 km with a peak at around 82km. ref

However, there is little known about the MSP composition except from extinction estimates based on satellite observations (Hervig et al., 2012) and material work function estimates based on rocket observations (Rapp et al., 2012). Due to their altitude location, rocket experiments with built-in dust probes are the only means of in-situ measurements. Mesospheric dust particles are located too high for high-altitudes balloons and too low for satellites. There have been several attempts to collect the mesospheric dust with probes on rockets, but no conclusive results have been reported from their subsequent laboratory analysis so far. Early collection experiments to study ice particles in NLC were made with large detectors where aerodynamics was seen as a limiting parameter for the detection of small particles. For instance, it has been reported that the median diameter size of particles that can be collected with their instrument is 130 nm and most of the analysed particles had diameters between 100 nm to 200 nm (Farlow et al., 1970). They pointed out, however, that their optical analysis had missed a large number of small particles on the collector. More recently, attempts to directly capture MSP from rocket were made with the MAGIC (Mesospheric Aerosol – Genesis, Interaction and Composition) instrument; those were based on reducing the collector size to the order of the molecular mean free path in order to minimize atmospheric shock effects due to the airflow around the payload (Hedin et al., 2014). In this paper, a new approach is considered as the design of the instrument aims at taking into account the modification of the dust particles during the collection process. Motivated by observations that the ice particles in the mesosphere contain smaller MSP, we aim to collect large IPs, in order to study the smaller MSP that they contain. Accordingly, a new sample collector is currently under development, the MEteoric Smoke Sampler MESS (Havnes et al., 2015). Instead

50 of trying to directly capture MSP, this instrument aims at collecting large dust particles that are not strongly deflected in the airflow; that is large MSP and ice particles, containing a certain percentage of MSP.

This current work aims at presenting the concept of the MESS instrument in order to evaluate the trajectories of dust particles inside the instrument until they reach the collection area and estimate its collection efficiency. The paper is organized as follows. Section 2 presents the design of the instrument. Section 3 describes the model that is used to evaluate the trajectories of dust

55 particles. Section 4 is dedicated to the presentation of the results, including the airflow in the vicinity of the instrument, the dust particles trajectories and the collection rates for different altitudes and rocket velocities, as well as a discussion about the final temperature and final speed of the dust particle. Finally, the conclusions and outlooks are drawn in Section 5, in particular by looking into the most suitable rocket conditions for an optimized collection of dust particles.
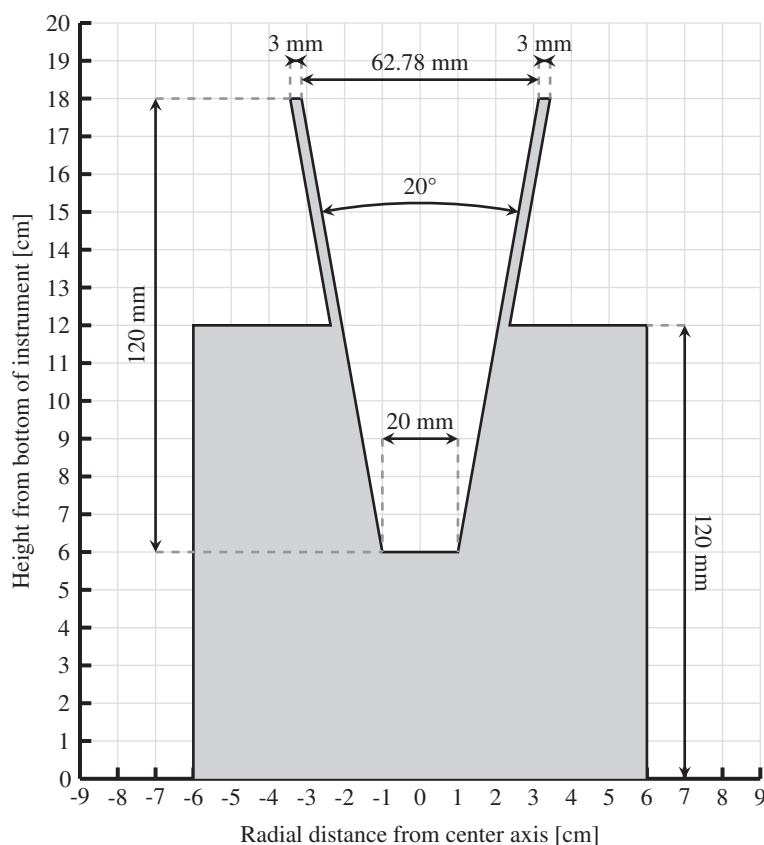
2 Instrument design

60   MESS is a rocket instrument intended to collect dust particles in the mesosphere. It will sit on the top deck of the rocket and
be exposed to the airflow caused by the rocket motion, which will carry the particles into the instrument. The experiment idea,
first proposed in Havnes et al. (2015), is to collect large ice particles less influenced by the airflow around the payload and
increase the amount of collected material by building the instrument with a funnel. Figure 1a shows the mechanical drawing of
MESS. The top shows a side view, where the lid can be seen as an extension of the funnel when opened. Because of the conical

65   shape, it will be possible to collect fragments from the entire funnel area. Dimensions are limited by other dust detectors in the
strawman payload, which also need to be exposed to the direct flow of air and dust. Figure 1b shows the simplified instrument
used in the simulations. The funnel opening has a diameter of 62.78 mm with a cone angle of 20°, corresponding to an opening
area of $A_{opening}$=3096 mm^2. The funnel height is 120 mm, and the total height of the instrument is 180 mm. The bottom of
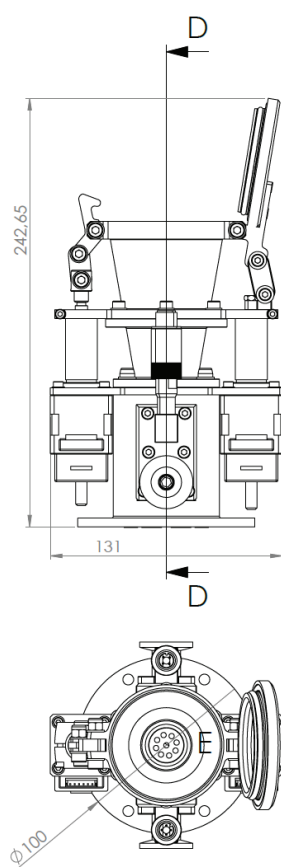
(a) Technical drawing of the MESS detector   (b) Simplified drawing of the MESS detector used in the simulations

Figure 1. Drawings of the MESS detector

the funnel is 20 mm in diameter, corresponding to a collection area of A_{coll}=314 mm^2. The funnel increases the sampling area

70 by $\sim$ 10. The collection area will consist of 8 TEM (Transmission Electron Microscope) grids distributed in a circle, as seen in the center of the bottom of Figure 1a. Identical reference grids will be located inside the instrument, not exposed to the airflow. TEM grids include a support mesh and a carbon foil, they are used in standard sample holders, and using them would facilitate easy handling of the samples. Note that TEM grids were also used in the MAGIC campaign Hedin et al. (2014). The instrument will be sealed by a mechanical lid which will be opened shortly after the nose cone ejection and kept open until the

75 apogee. A pressure valve is located inside the instrument, keeping the pressure similar to the pressure at the opening altitude. At mesospheric altitudes, the air density is still significant, and rocket speeds are in the order of $\sim 1000 \, \mathrm{ms}^{-1}$, consistent with supersonic speeds. As a result, a bow shock will form in front of the instrument, which will affect the airflow and cause deflection of the particles. The effect of this deflection will be addressed in this paper.

3 Model description

80 In order to evaluate the trajectories of the dust particles in the instrument, their equation of motion have be modeled. Accordingly, the modeling of the dust particles dynamics is presented in Section 3.1. As the dust particles dynamics is mainly driven by the drag force that they undergo and that depends on the characteristics of the background gas, Section 3.2 then presents the evaluation of the airflow. Finally, we assume here that dust particles can break up when they collide with the funnel wall of the instrument and the model assumptions on the fragmentation process are introduced in Section 3.3.

85 ### 3.1 Dust particle dynamics

We assume that the mesospheric dust of large size is primarily water ice particles that contain a smaller amount of MSP. In this work we assume they contain 3% of MSP and 97% of ice and that the latter determines the bulk properties. We assume in addition that small particles can be pure MSP. We assume that dust particles are perfectly spherical, with a radius r_d and a mass density ρ_d. Then, the dust particles are assumed to be neutral, electric and magnetic effects can be neglected they are

90 only subjected to gravity and drag. This latter comes from the collisions between the molecules of the background gas and the dust particles. It is incidentally assumed that the dust particles are by far more massive than the gas molecules. Finally, the dust particles are heated due to these collisions and can sublimate, making necessary the consideration of their mass variation. As a consequence, by taking the rocket as the reference frame, the equation of motion of dust particles having a velocity $\vec{v}_d$ can be written as follows (Baines et al., 1965; Smirnov et al., 2007; Antonsen and Havnes, 2015) :

95
$$\frac{d\vec{v}_d}{dt} = \frac{1}{m_d}\left[m_d\vec{g} + \chi\pi r_d^2 m_g n_g v_{th,g}^2 f(u)\frac{\vec{v}_g - \vec{v}_d}{|\vec{v}_g - \vec{v}_d|} - \frac{dm_d}{dt}\vec{v}_d \right] \tag{1}$$

with $m_d = 4\pi\rho_d r_d^3/3$. In the right hand side, the first term corresponds to gravity, with $\vec{g}$ the gravity acceleration, the second term corresponds to the drag force and the third term corresponds to the mass variation of the dust particles. Regarding the drag force, the parameter χ is associated to the geometry of the dust particles; for spherical dust particles $\chi = 1$. m_g, n_g and $v_{th,g}$ respectively correspond to the molecules mass, density and thermal speed of the background gas. The thermal speed is

defined by $v_{th,g} = \sqrt{2k_B T_g / m_g}$ with k_B the Boltzmann constant as a function of the temperature of the background gas T_g. The function f is given by :

$$f(u) = \frac{1}{\sqrt{\pi}} \left(u + \frac{1}{2u} \right) e^{-u^2} + \left(1 + u^2 - \frac{1}{4u^2} \right) \mathrm{erf}(u) \tag{2}$$

in terms of the relative speed $u = \left| \vec{v}_g - \vec{v}_d \right| / v_{th,g}$ assuming specular reflection of background gas molecules during collisions with dust particles. This allows a modeling of the drag force valid for both subsonic and supersonic regimes. Because of the heating of the dust particles which can sublimate, the evolution of the dust particles temperature T_d has to be modeled. It is given by the energy balance that can be written as follows (Horányi et al., 1999; Antonsen and Havnes, 2015) :

$$\frac{dT_d}{dt} = \frac{1}{m_d c_d} \left(\frac{\pi}{4} r_d^2 n_g v_{th,g} k_B T_g g(u) - L_d \frac{dm_d}{dt} \right) \tag{3}$$

with c_d and L_d the dust particles specific and latent heats respectively. The first term of the right hand side corresponds to the heating due to collisions with background gas molecules and the second corresponds to the modification of the internal energy due to the sublimation energy. Similarly to Eq.(1), the function g is defined as a function of the relative speed u and is given by :

$$g(u) = \frac{2}{\sqrt{\pi}} \left(5 + 2u^2 \right) e^{-u^2} + \frac{3 + 12u^2 + 4u^4}{u} \mathrm{erf}(u) \tag{4}$$

so that the modeling the heating of dust particles is valid for both subsonic and supersonic regimes. It can be pointed out that radiative processes, such as thermal emission of the dust particles, solar radiation and terrestrial radiation, are neglected in Eq.(3) (Rizk et al., 1991).

The mass variation of the dust particles $d_t m_d$ appearing in Eq. (1) and Eq. (3) associated to their sublimation corresponds to a flux of molecules constituting the dust particles out of their surface. Thus, the mass variation of the dust particles is defined by :

$$\frac{dm_d}{dt} = -4\pi \rho r_d^2 \frac{dr_d}{dt} \tag{5}$$

where the radius variation is evaluated by assuming that dust particles molecules leave the surface diffusively. It is given by the Hertz-Knudsen equation (Skorov and Rickman, 1995; Kossacki and Leliwa-Kopystynski, 2014; Antonsen and Havnes, 2015) which can be written as :

$$\frac{dr_d}{dt} = -\frac{P_{vap}}{\rho_d} \sqrt{\frac{m_D}{2\pi k_B T_d}} \tag{6}$$

with m_D the mean mass of dust particles. P_{vap} corresponds to the vapor pressure and is given by (Podolak et al., 1988) :

$$P_{vap} = P_0 \exp\left(-\frac{T_0}{T_d} + \frac{2\gamma_d m_D}{\rho r_d k_B T_d} \right) \tag{7}$$

where P_0 and T_0 are constants depending on the type of dust particles, i.e. ice particles or MSP. The second term in the exponential corresponds to a correction of the vapor pressure so that spherical mass ejection for very small surfaces is considered (Evans, 1994). This correction term is given in terms of the specific surface energy γ_d of the dust particles.

3.2 Airflow model

130   In order to calculate the trajectories and the heating of the dust particles, the density, the temperature and the velocity of the background gas have to be evaluated. Such an evaluation is done by using the DS2V program developed by Bird and Brady (1994). It is a 2D numerical software based on Direct Simulation Monte Carlo (DSMC) methods which are commonly used to study rarefied gas dynamics. The mesosphere and the lower thermosphere are characterized by a Knudsen number usually between 0.01 and 1, this corresponds to a rarefied gas (Antonsen and Havnes, 2015). The Navier-Stokes equations which are

135   suitable for a continuous flow (when $Kn \ll 0.1$) can not be used anymore and probabilistic methods should be preferred.

3.3 Fragmentation model

Because of the conical shape of the detector, a large number of the incoming dust particles can collide with the funnel walls. We assume that MSP are reflected, while the ice particles break into fragments. This fragmentation process is unknown, to estimate it, we refer to results (Tomsic et al., 2003) from laboratory and simulation studies. In their ice collision experiments

140   and molecular simulations Tomsic et al. found that a large fragment is likely to be created during the collision of pure ice particles onto a metal wall with a large angle with respect to the normale direction of the surface (Tomsic et al., 2003).
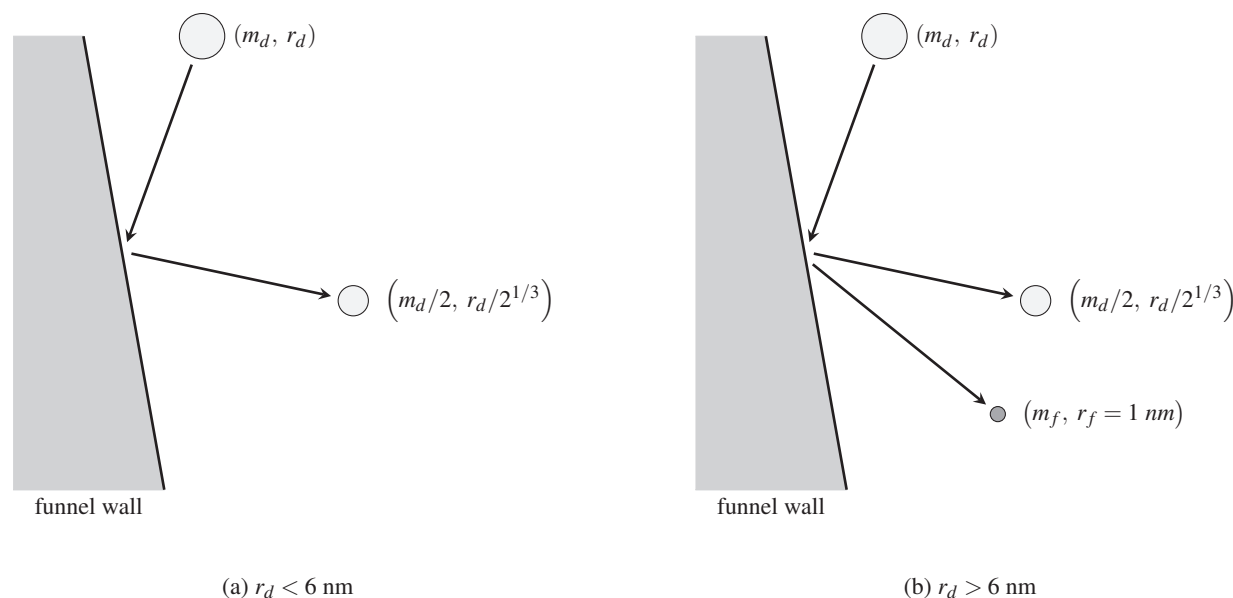

(a) $r_d < 6$ nm   (b) $r_d > 6$ nm

Figure 2. Drawing of the modeling of the dust particles fragmentation having a mass m_d and a radius r_d when they collide with the funnel wall. The size scales are not respected for the sake of clarity. When $r_d > 6$ nm, the angle associated to the two fragments is the same and corresponds to the angle of the incident particle with respect to normale direction of the surface. Different angles are displayed for the sake of clarity.

Accordingly, it is assumed for our case that a large fragment is created having a mass equal to half of the mass of the incoming dust particle and the same composition as the incoming dust particle, i.e. 3% of MSP and 97% of ice. The other half of the mass is divided between a large number of smaller fragments. They are assumed to be small enough so that the ice sublimates immediately. According to the mass conservation and by assuming that the radius distribution $\omega(r)$ the MSP fragments scale as $\omega(r) \propto r^{-3}$ as supported by results from in-situ measurements (Antonsen et al., 2020). It can be deduced that the mean radius of these fragments is mostly smaller than 0.8nm, see Appendix A. This implies that the model presented in the previous section does not track any MSP fragments. Finally, the description of the fragmentation process that is used in this work to investigate the trajectories of the MSP fragments is summarized in Figure 2. We consider only the large fragment if $r_d < 6$ nm right before the collision, and we consider the large fragment plus one MSP fragment having a radius of 1nm if $r_d > 6$ nm right before the collision. For both particles, the angle after collision is the same as the angle of the incident particle due to specular reflection.

4 Results

This section is dedicated to the presentation of the results coming from simulations performed for different altitudes and different rocket speeds.The altitudes of 80 km, 82 km, 85 km and 90 km are considered as they correspond to the borders and centers of the region of interest as seen in Section 1. The rocket velocity varies with the altitude and depends on the rocket apogee. For a mesospheric rocket, the apogee lies between 110 to 130 km and it can be expected a speed around 1000 m.s^{-1} at an altitude between 80km and 90km. Accordingly, rocket speeds of 800 m.s^{-1}, 1000 m.s^{-1} and 1200 m.s^{-1} are considered. First in Section 4.1 the airflow of the background gas in the vicinity of the instrument is derived. Then, the trajectories of dust particles will be presented in Section 4.2 with two illustrative examples. In order to evaluate in a more comprehensive way the dust particles motion in the instrument, the detection rates will be presented in Section 4.3 for the different altitudes, different rocket velocities and different dust particles initial radii. These detection rates will be then used to estimate the mass of dust particles collected during a rocket flight. Finally, the final temperatures and speeds of the dust particles when they reach the collection area will be presented in Section 4.4 and Section 4.5 respectively.

4.1 Neutral gas flow

The flow of the background gas around the rocket depends on its density and temperature. These parameters, and in particular the density, can vary over short spatial and temporal scales. Variations by roughly a factor of 2 were observed for the density during previous rocket campaigns (Lübken et al., 1993; Strelnikov et al., 2003). However, such variations are neglected in a first approximation and because it is out of the scope of the present work. Thus, mean values provided by the MSIS-E-90 atmospheric model are used (Chulaki, 2020) to evaluate the initial densities and temperatures of the background gas. These values are summed up in the Table 1 for the four different altitudes.

Altitude [km]	80	82	85	90
Density $[\mathrm{m}^{-3}]$	5.909×10^{20}	4.115×10^{20}	2.220×10^{20}	6.697×10^{19}
Temperature [K]	160.5	150.0	139.4	138.7

Table 1. Initial densities and temperatures of the background gas for the four different altitudes coming from the MSIS-E-90 model(Chulaki, 2020).

The Figures 3, 4, 5 and 6 show the densities and the streams of the background gas around the detector for 80 km, 82 km, 85 km and 90 km respectively and for the three different rocket speeds in each case. It can be seen that a bow shock is created at the top of the detector, with a thickness of about 4cm. This is because the rocket speed is always higher than the sound speed of the background gas. The gas density in the bow shock is higher than the initial density by a factor of 3 to 4 depending on the rocket speed. Below the bow shock, the gas density reaches its highest value in the funnel, where it is higher than the initial density by about one order of magnitude depending on the rocket speed. The increase of the gas density in these two regions
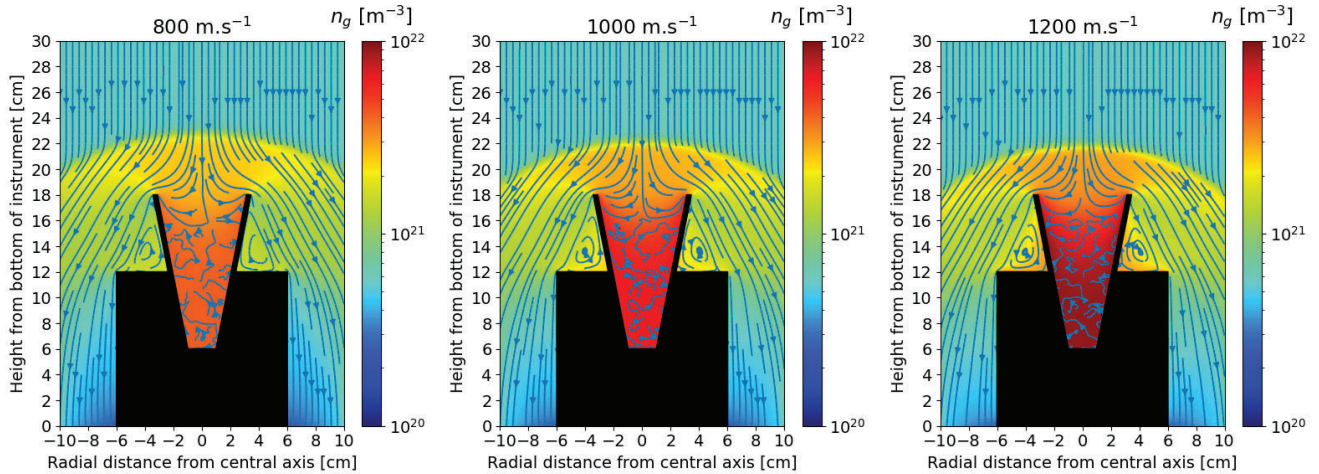
Figure 3. DSMC results for 80km showing the background gas density n_g and stream around the detector for 800 m.s^{-1}, 1000 m.s^{-1} and 1200 m.s^{-1} rocket speeds
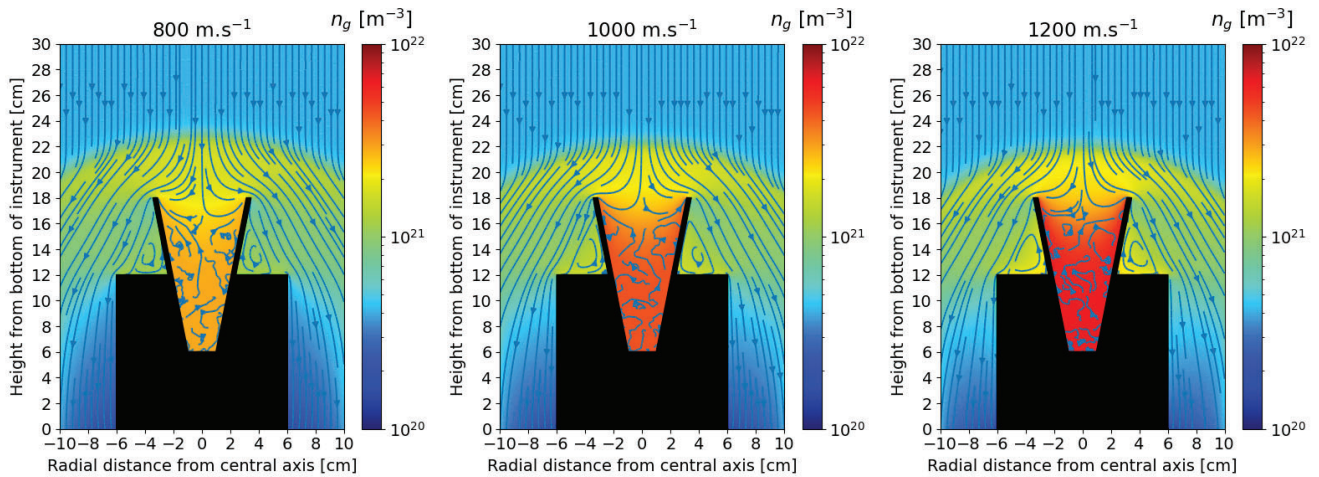

Figure 4. DSMC results for 82km showing the background gas density n_g and stream around the detector for 800 m.s^{-1}, 1000 m.s^{-1} and 1200 m.s^{-1} rocket speeds

implies that the dust particles can be slowed down by undergoing the drag force twice, first during the bow shock crossing and then, and in a more important way, when being inside the funnel. When looking at the influence of the rocket speed on the gas density for a given altitude, it appears that the gas density of the bow shock and inside the detector gets higher with the rocket speed, which means that a higher rocket speed leads to a stronger drag force. Thus, increasing the rocket speed does
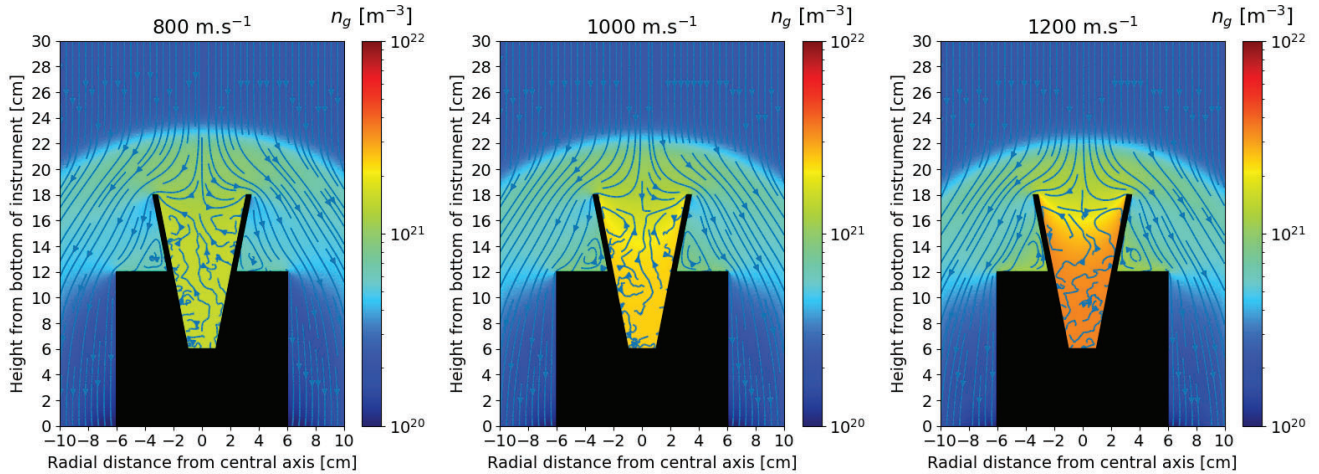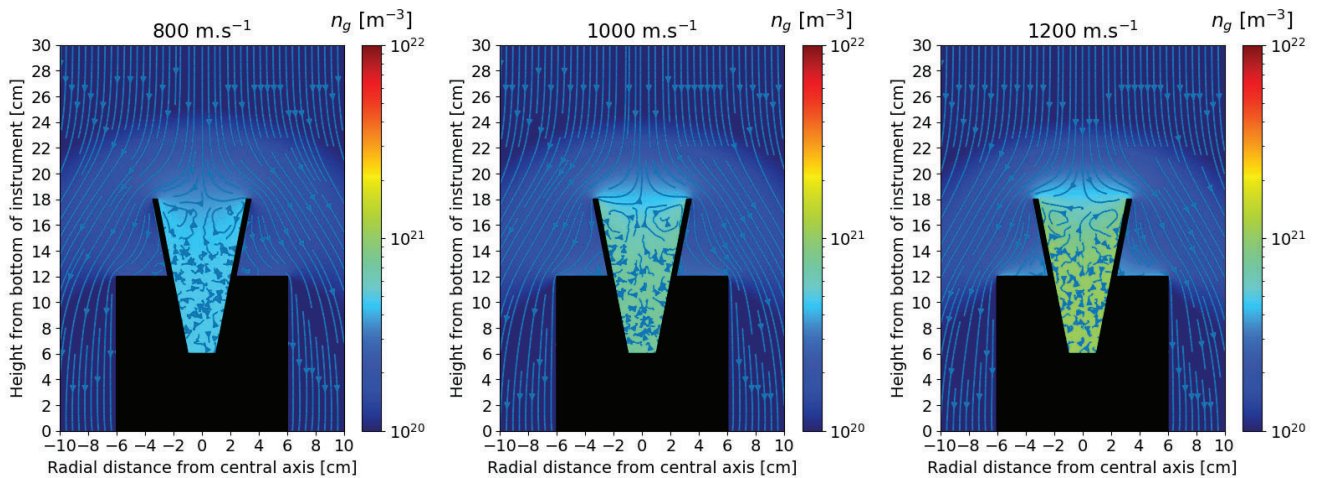
Figure 5. DSMC results for 85km showing the background gas density n_g and stream around the detector for 800 m.s^{-1}, 1000 m.s^{-1} and 1200 m.s^{-1} rocket speeds

Figure 6. DSMC results for 90km showing the background gas density n_g and stream around the detector for 800 m.s^{-1}, 1000 m.s^{-1} and 1200 m.s^{-1} rocket speeds

not necessarily entail a more efficient collection of dust particles as they would influenced more strongly by the drag force and possibly decelerated more than for the lower rocket speed. This will be addressed in Section 4.3 Finally, it can be observed that the stream is mainly laminar around the detector but becomes turbulent inside the detector which means that the trajectories of the dust particles may be modified because of these turbulence. Given the slow-down that dust particles can experience when

185 crossing the bow shock or being in the funnel and given the turbulence taking place in the detector, it can be expected that a significant fraction of the small particles do not reach the collector.
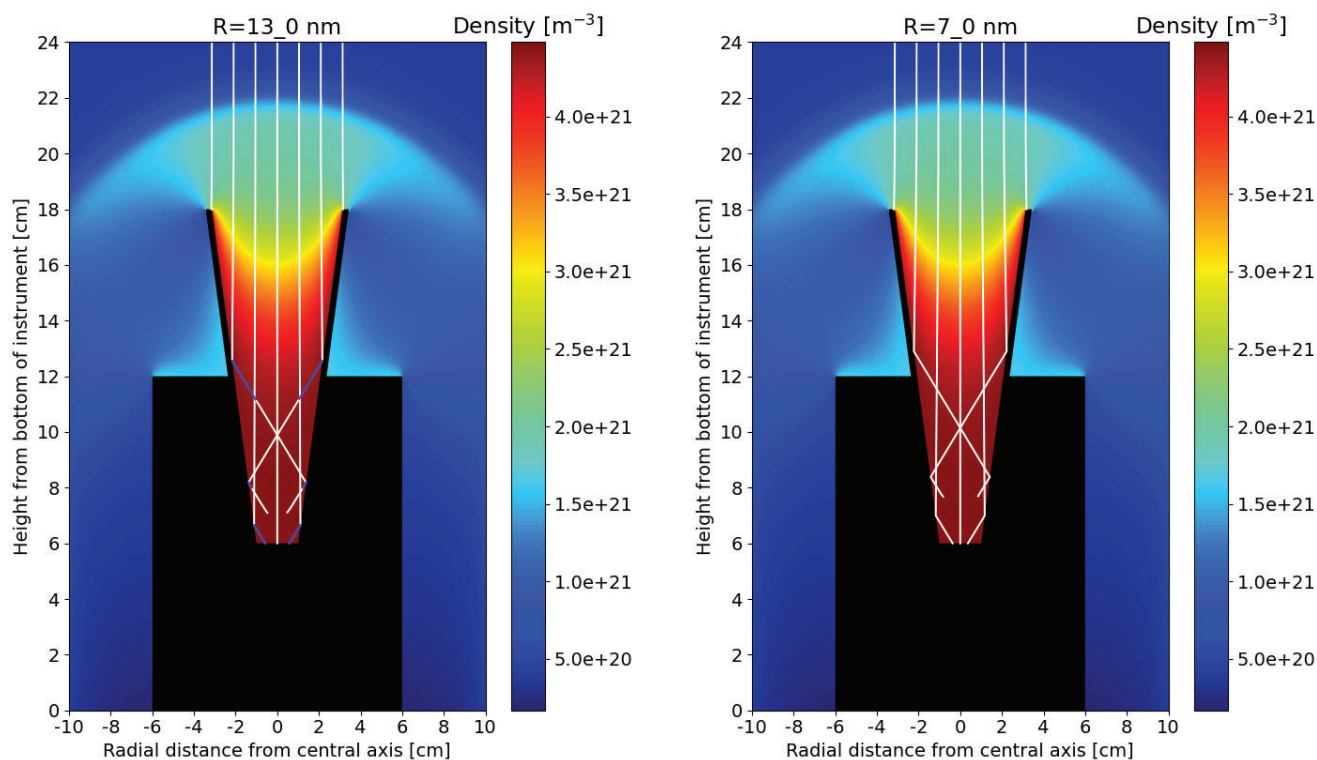
4.2 Dust particle trajectories

The previous results providing the airflow of the background gas in the vicinity of the instrument can now be used to evaluate the motion of the dust particles. To do so, equations (1)-(6) are solved numerically using the 4th order Runge-Kutta method.

190 These equations are function of the mass density ρ_d, the specific heat c_d, the latent heat L_d, the mean mass m_D and the specific surface energy γ_d of dust particles that are different for ice particles and MSP. The values of these parameters are gathered in Table 2 for both ice particles and MSP (Podolak et al., 1988; Antonsen and Havnes, 2015). This section aims at presenting the results obtained from these simulations for both ice particles and MSP through the evaluation of their trajectories. For the sake of clarity, it has been chosen to present only one representative example for both ice particles and MSP showing the typical

195 trajectories of the dust particles in the instrument instead of an exhaustive list. To investigate the trajectories of the dust particles in a comprehensive way, the evaluation of the trajectories should be done for different altitudes, different rocket velocities and different initial radius leading to the very large number of cases. The presentation in the next section of the collection rates as a function of these parameters aims at addressing this question and study the efficiency of the instrument for different altitude and rocket speeds.

	ρ_d $\left[\text{kg.m}^{-3}\right]$	c_d $\left[\text{J.kg}^{-1}.\text{K}^{-1}\right]$	L_d $\left[\text{J.kg}^{-1}\right]$	m_D [a.m.u.]	P_0 $\left[\text{J.m}^{-3}\right]$	T_0 [K]	γ_d $\left[\text{J.m}^{-2}\right]$
Ice particles	980	$90+7.5T_d$	2.78×10^6	18	3.9×10^{11}	4845	0.19
MSP	3000	1000	6×10^6	140	1.5×10^{13}	56655	0.20

Table 2. Values of the parameters for ice particles and MSP. It is reminded here that P_0 and T_0 do not represent the pressure or the temperature of any dust particles but they are constants that have the dimension of a pressure and a temperature. rho_d is..., C_d is,... etc.

200 Figure 7 shows the trajectories of ice particles that have an initial radius of 13nm and MSP having an initial radius of 7nm. Different cases can be identified. First, dust particles starting near the central axis of the instrument. It can be seen that an ice particle with an initial radius of 13nm and a MSP with an initial radius of 7nm cross entirely the instrument and reach the collection area. However, if some dust particles are smaller and lighter, they are likely not to reach the collection area. They are slowed-down because of the drag force and will eventually float in the instrument. This leads to a minimum initial radius above

205 which dust particles should always reach the collection area. The largest value is reached for the highest rocket speed and the lowest altitude as it corresponds to the most important increase of the gas density in the bow shock and in the funnel, i.e. for a rocket speed of 1200 m.s^{-1} and an altitude of 80km. In that case, the minimum initial radius is about 11nm for ice particles, and is about 9nm for MSP. Then dust particles starting a bit farther from the central axis. They enter the instrument and, if they are large enough, collide with the funnel wall otherwise they are progressively stopped by being slowed down due to the drag

210 force. In the case of an ice particle, the collision leads to a rebound during which the radius of the ice particle is divided by a

(a) Ice particles with an initial radius of 13nm. The white lines represent the ice particle trajectories. The blue lines represent the trajectories of the fragments constituted of pure MSP created during each collision of an ice particle with a funnel wall.

(b) MSP with an initial radius of 7nm.

Figure 7. Trajectories of ice particles and MSP in the MESS instrument for rocket velocity of 1000m.s^{-1} and an altitude of 82km.

factor of $2^{1/3}$ and a formation of a fragment constituted of pure MSP as it can be observed on Figure 7a In the case of a MSP, the collision only leads to a rebound as it can be seen on Figure 7b. In both cases, starting relatively far from the central axis means that dust particles can bounce several times and travel over a larger distance than a dust particle starting near the central axis. They undergo the influence of the drag force during a longer time and are more slowed down. Moreover, ice particles

215 colliding several times see their radius divided by a factor of $2^{1/3}$ at each collision, become smaller and slowed down more importantly by the drag force. Therefore, it is possible that they don't reach the collection area. In addition, fragments resulting from the collision of an ice particle with a funnel wall are quickly slowed down as they are very small, ∼1nm, and only those created near the collection are likely to reach it, otherwise they will float in the instrument. Finally, dust particles starting far from central axis of the instrument. These particles can not be collected as they are either taken away by the airflow or hit the

220 top of the funnel. For ice particles in that case, they will explode in a huge number of small fragments. Unlike the collisions

13

that are considered in the fragmentation process presented in Section 3.3, the collision here is head-on and any large fragment is created. All of the fragments are small and are taken away by the airflow, even those heading toward the central axis of the instrument, because of the stream existing in that region, see Figure 3 to Figure 6.

As a conclusion, it appears from Figure 7 that particles entering the instrument are either slowed down and float in the
225 instrument or reach the collection area. The case where particles entering the instrument and then go out be being taken away the airflow, as it could have been expected when looking at the streams, especially on Figure 3 and Figure 4, does not happen. In addition, it was observed when looking at the streams that turbulence take place in the instrument. But it appears that these turbulence don't have any influence of the dust particles trajectories. These conclusions are drawn by evaluating the trajectories of ice particles and MSP having an initial radius of 13nm and 7nm respectively. However, they can be generalized to other
230 radius. Even though trajectories of dust particles having a different initial radii are not shown here for the sake of clarity, simulations have been performed to evaluate the trajectories of dust particles that have an initial radius ranging from 1nm to 20nm for ice particles and ranging from 1nm to 10nm for MSP. The particles tracking in the simulation is stopped either when the particle reaches the detector, or when the particle is no longer in the simulation box, i.e. the particle is taken away from the instrument by the airflow and does not reach the detector, or when the particle is stopped due to the slowing down coming from
235 the drag force. i.e. the particle does not reach the detector, or, for ice particles, when the particle radius becomes smaller than 0.8 nm where the model is no longer valid. In that case, the particle does not reach the detector as it is completely sublimated.

4.3 Collection rates

It has been observed in last section that when entering the instrument some of the dust particles can reach the bottom of the instrument and be collected but others are sufficiently slowed down to be stopped and eventually float in the instrument.
240 This section is dedicated to the presentation of the rates of the ice particles and MSP reaching the collection area. These rates are calculated by calculating the ratio between the number of particles reaching the collection area and the number of particles entering the instrument for different initial radius, different rocket speeds and different rocket. In each case, about 150 particles are considered as a compromise between a number large enough to be relevant for statistics and a number not too large regarding computational capabilities.
245 Figure 8 shows the collection rates of ice particles as a function of their initial radius, corresponding to the number of particles reaching the collection area at the bottom of the instrument. They are shown for different rocket speed, 800 m.s^{-1}, 1000 m.s^{-1}, 1200 m.s^{-1}, and different altitudes, 80km, 82km, and 85km. As mentionned in Section 1, most of the ice particles are located between 80km and 85km with a peak around 82km. Similarly, Figure 9 shows the collection rates of MSP as a function of their initial radius. They are shown for different rocket speed, 800 m.s^{-1}, 1000 m.s^{-1}, 1200 m.s^{-1}, as for ice
250 particles, and different altitudes, 80km, 85km, and 90km, which are different for the altitudes considered for ice particles. As seen in Section 1, most of the MSP are located between 80km and 90km with a peak around 85km.

Overall conclusions are basically the same for both ice particles and MSP. First, it can be observed than the collection rates increase with the initial radius. Larger dust particles are more likely to reach the collection area as their trajectories are less influenced by the drag force. Then it can be seen that the collection rates are more important for larger altitudes and smaller
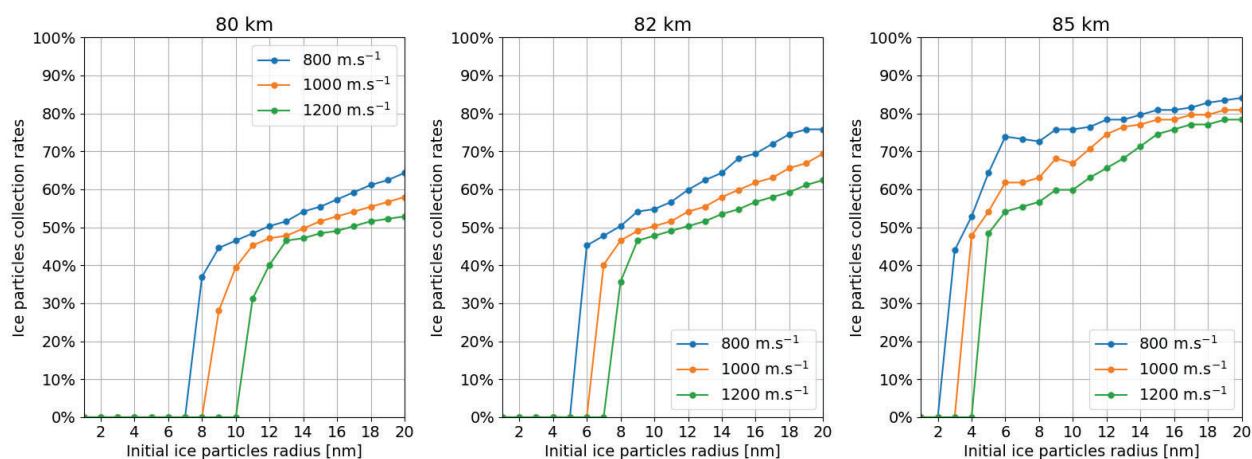
Figure 8. Ice particles collection rates as a function of their initial radius for three different rocket speeds 800 m.s^{-1}, 1000 m.s^{-1} and 1200 m.s^{-1} and three different altitudes 80km, 82km and 85km. Each point of the graphs has been obtained by calculating the trajectories of about 150 ice particles.
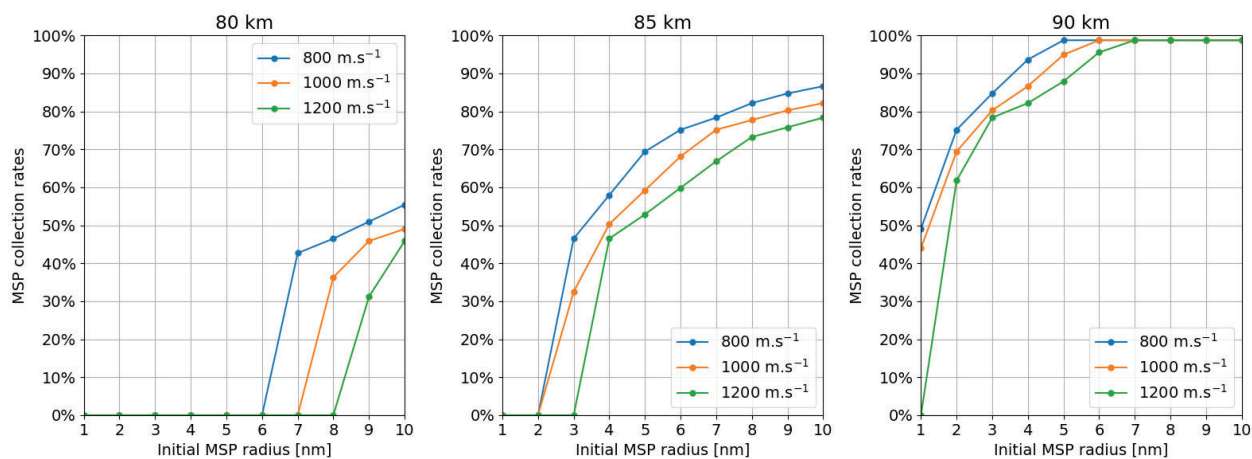

Figure 9. MSP collection rates as a function of their initial radius for three different rocket speeds 800 m.s^{-1}, 1000 m.s^{-1} and 1200 m.s^{-1} and three different altitudes 80km, 85km and 90km. Each point of the graphs has been obtained by calculating the trajectories of about 150 MSP.

rocket speed. At higher altitudes, the density of the background gas is smaller leading to a weaker drag force, this latter can be assumed as proportional to the background density in a first approximation, see Section 3.1, and a larger number of particles are likely to reach the collection area. Similarly, it appears that a slower rocket leads to a more efficient collection of IP. Although

15

it could be expected that a faster rocket would lead to a better collection because it would lead to faster crossing of the bow shock and the instrument and a shorter influence of the drag force, it rather appears that the IP trajectories are more driven by

260 the drag force. This answers the question on the competition between drag force and initial particles speed raised in Section 4.1. Finally, it can be observed that particles under a certain size don't reach the collection area. This creates a sort of threshold radius which is between 2nm and 10nm for IP and between 1nm and 8nm for MSP depending on the rocket speed and altitude. A smaller rocket speed or a lower altitude leads to a weaker drag force allowing smaller particles to reach the collection area. Such an effect may have to be considered during the design of the rocket mission with respect to the apogee. Those particles

265 having a radius smaller than the threshold radius are slowed down and stopped in the instrument and eventually float. Even these particles don't reach the collection area, they could still be collected when the closing system is activated as they would remain inside the instrument. Thus, the instrument will have to open with caution during the sample analysis so that these particles can't escape. In addition, the walls of the funnel should be inspected as dust particles could be stuck to them. Overall, it appears that the instrument presented in this work can collect dust particles over a large range of size. This instrument should

270 collect in a efficient way IP larger than 10nm and MSP larger than 8nm. In addition, it should be able to collect a significant number of IP larger than 2nm and MSP larger than 1nm, even though the collection rates are the most important at the highest altitude where dust particles are less numerous (Megner et al., 2006; Baumann et al., 2013).

4.4 Estimate of the final temperatures

During their entry in the instrument, dust particles can be heated until undergoing mass ablation. This heating that cannot be

275 avoided with the current rocket speed may lead to modification of the chemical composition of the dust particles which would complicate the laboratory analysis.. This section aims at addressing this question by looking at the final temperature of the dust particles, i.e. when they reach the collection area.

Figures 10 and 11 show the final temperatures of ice particles and MSP respectively as a function of their initial radius for the three rocket speeds 800 m.s^{-1}, 1000 m.s^{-1} and 1200 m.s^{-1}, and different altitudes. Similarly to last section, final temperature

280 of ice particles is shown for an altitude of 80km, 82km and 85km, and final temperatures of MSP is shown for an altitude of 80km, 85km and 90km. The final temperatures correspond to those of the particles when they reach the collection area. The profiles therefore start from the threshold radius. The particles that are considered here are those starting in the central axis of the instrument for purpose of illustration. It has been checked that there are no relevant variations of the final temperature depending on their initial position. In addition, ice particles starting at the center are those that are heated the most, which

285 should provide the upper limit of the dust particles final temperatures. We can see for ice particles that there is no drastic change in the final temperature. The largest difference is about 25K overall between 170K and 195K. The heating due to the drag force leads to a melting of the outer surface of the ice particles that remains relatively cold. The fact that the final temperature range from 170K to 190K also means that crossing the instrument results in a relatively small increase of their temperature. It is about a few tens of kelvins as the initial temperature is between about 140K and 160K, see Section 4.1. This

290 means that the MSP located inside the ice particles are not heated during their collection and the ice can be considered as acting like a thermal shield. Finally, the trends as a function rocket speed and altitude are once again due to the drag force. A lower

16

altitude and a faster rocket are associated to a stronger drag force resulting in a more important heating. Concerning pure MSP, it can be seen they are heated significantly, up to 1800K. Although the first term in Equation 3 associated the heating induced by the drag force is about the same order of magnitude for MSP and ice particles, the second term associated to the mass

295 variation is much smaller for MSP than for ice particles. The parameter T_0 taking part of the expression of the vapor pressure that is used to evaluate the mass variation is very different between MSP and ice particles. One has $T_0 = 56655$K for MSP and $T_0 = 4845$K for ice particles leading to a difference by a factor about 10. Thus, for MSP, the heating is not counterbalanced by the mass variation and MSP can reach large temperatures. This especially means that the MSP chemical composition can be altered during their crossing of the instrument and the chemical composition of MSP reaching the collection can be different

300 to the chemical composition of MSP before they enter the instrument, i.e. those that are present in the mesosphere. Note that these high temperature are also higher than the temperature that can be reached bu the collection area during its re-entry of the rocket in the atmosphere. Finally, it appears that a slower rocket and a higher altitude lead to a final temperature that is significantly smaller. This can thus be an additional reason to prefer slower rockets as they are less likely to induce a change in the chemical composition of MSP.

305 **4.5 Estimate of the final speeds**

When reaching the collection area, the dust particles have a nonzero speed. Depending on that speed, the dust particles may damage the TEM grids, the walls of the collection area, and the instrument more generally. Additionally, they may also break up when eventually hitting the collection area. This section aims at addressing this question by looking at the final speed of the dust particles.
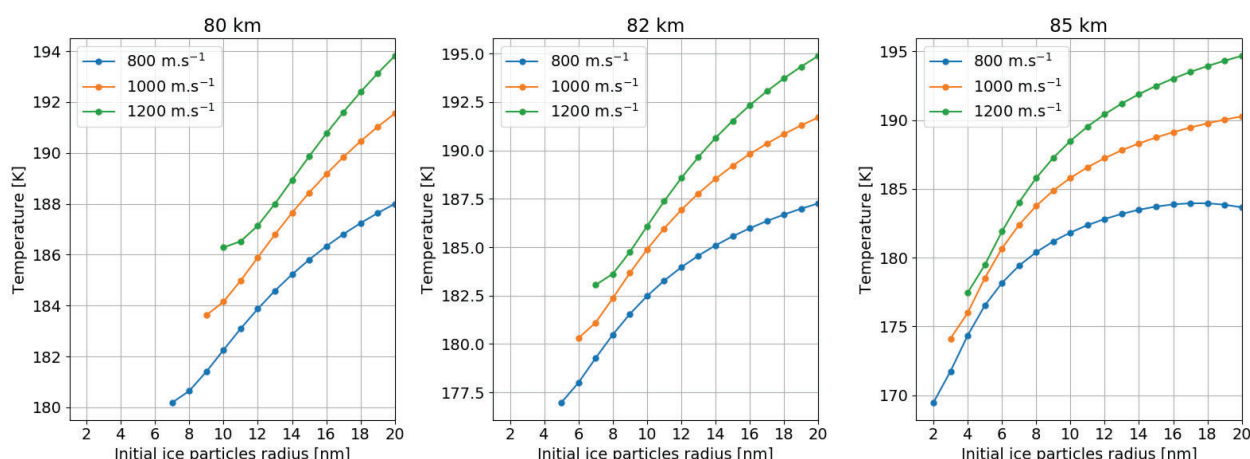

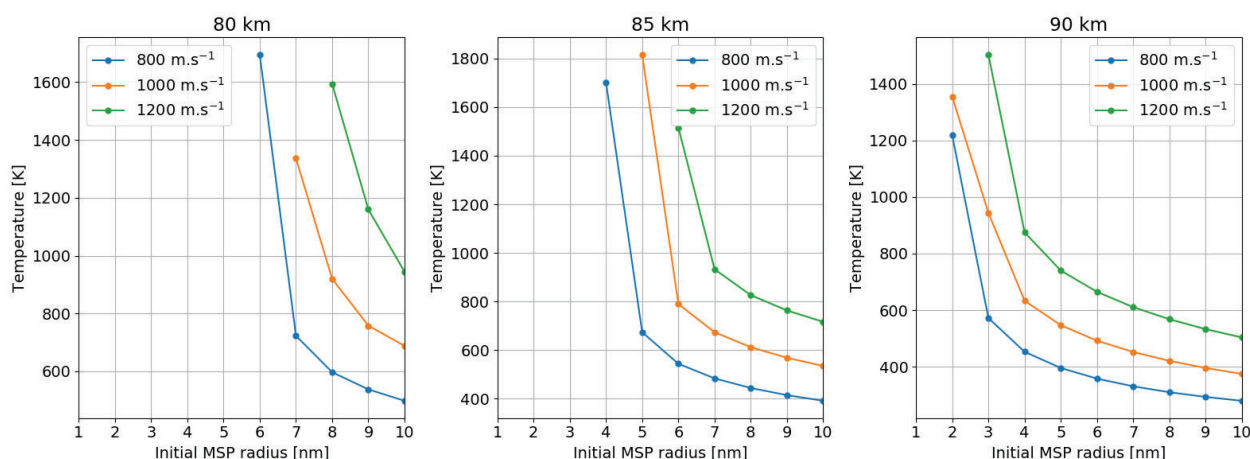**Figure 10.** Final temperature of ice particles when they reach the collection area

Figure 11. Final temperature of MSP when they reach the collection area

Figures 12 and 13 show the final speeds of ice particles and MSP respectively as a function of their initial radius, for the same rocket speeds and altitudes as previously. We can see that the final speed of ice particles and MSP quickly increases and most of the dust particles have a final speed of several hundreds of meters per second. This speed corresponds to the speed that dust particle have when entering the collection area. For low altitude, it can be seen that a slower rocket leads to larger final speed for the dust particles. Said differently, a faster rocket leads to a more efficient deceleration of the dust particles, which comes from the bow shock created by the rocket that is strong enough to slow down the dust particles efficiently. The faster the rocket, the stronger the bow shock and the more efficient deceleration of the dust particles. At higher altitudes, a slower rocket leads on the contrary to smaller final speeds. In that case, the density of the atmosphere is such that the bow shock created by the rocket is not strong enough to slow down larger dust particles. Then, the final speed will be driven by the rocket speed. Differently to the last section where it clearly appeared that slower rockets would be more beneficial, the situation seems more ambiguous here. A slower rocket would be more beneficial at higher altitude but a faster rocket would be more beneficial at lower altitude.

Figures 12 and 13 show the final speeds of dust particles starting in the central axis of the instrument. Unlike the final temperatures, the final speed of dust particles strongly depends on their initial position in relation to the central axis. Accordingly, Figures 14a and 14b show the profile of the final speeds along the radial direction of ice particles and MSP respectively. For ice particles, these radial profiles are shown for an altitude of 82km and an initial radius of 20nm. For MSP, the radial profiles are shown for an altitude of 85km and an initial radius of 10nm. In both cases, they are shown for the three rocket speeds 800 m.s^{-1}, 1000 m.s^{-1} and 1200 m.s^{-1}. It has been opted to show the profiles associated to only one altitude and one initial size as a purpose of illustration. The altitudes of 82km and 85km have been chosen as a mean altitude. The initial radii of 20nm and 10nm have been chosen because they correspond to the maximum radii which are considered in this work. Such dust particles should be the least decelerated leading the upper limit of the final speed.

4.6 Estimate of collected mass

With the caveat that the numbers are subject to great uncertainty, we now attempt to estimate the total mass of dust collected. For this we combine the detection efficiencies that we derived for the MESS instrument with published data on dust distributions. For estimating the total mass of directly collected MSP we apply a published number density profile (Baumann et al., 2013) from model calculations by Megner and collaborators (Megner et al., 2006); these data are for September atmospheric conditions, due to limitations of the published data. We also estimate the amount of collected MSP material that is contained in ice particles. The ice particle densities are based on observational and model data sets for the location of the Andoya rocket launch site (Kiliani et al., 2015) where number densities of ice particles are from UV, VIS and IR lidar observations of NLC (Baumgarten et al., 2007, 2010) and size distributions are from models (Berger and Lübken, 2015).

In both cases we follow the same approach for the estimate. For a given dust number density we describe the mass of collected particles is:

$$m_{collected} = A_{coll} \, \Delta h \, n_d \, V_{dust} \, \rho_{d,msp} \, \alpha \, \sigma \tag{8}$$

where $A_{coll}, \Delta h$ and V_{dust} are the collection area, sample altitude and volume of dust respectively. The dust volume given is $\frac{4}{3}\pi r_d^3$, assuming spherical particles, n_d is the dust number density, and $\rho_{d,msp}$ is the mass density of MSP. The collection efficiency σ depends on particle size, height and speed of the rocket as we investigated above. The filling factor ~~as~~ α denotes the fraction of dust mass that is MSP material contained in the ice particles and it is unity for MSP and 0.03 for the ice particles. We limit this estimate to the primary particles.

To estimate the collected MSP, we combine the published number densities for particles $\leq 5nm$ and the mean detection efficiencies we found for these sizes. In the same way, we estimate the collected MSP $> 5nm$. We sum up the contributions
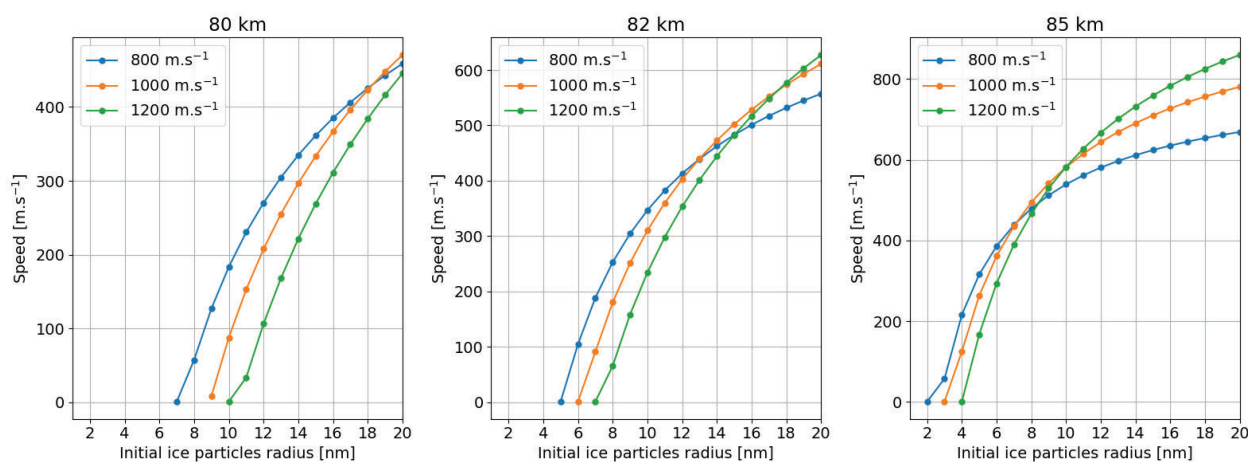

Figure 12. Final speed of ice particles when they reach the collection area
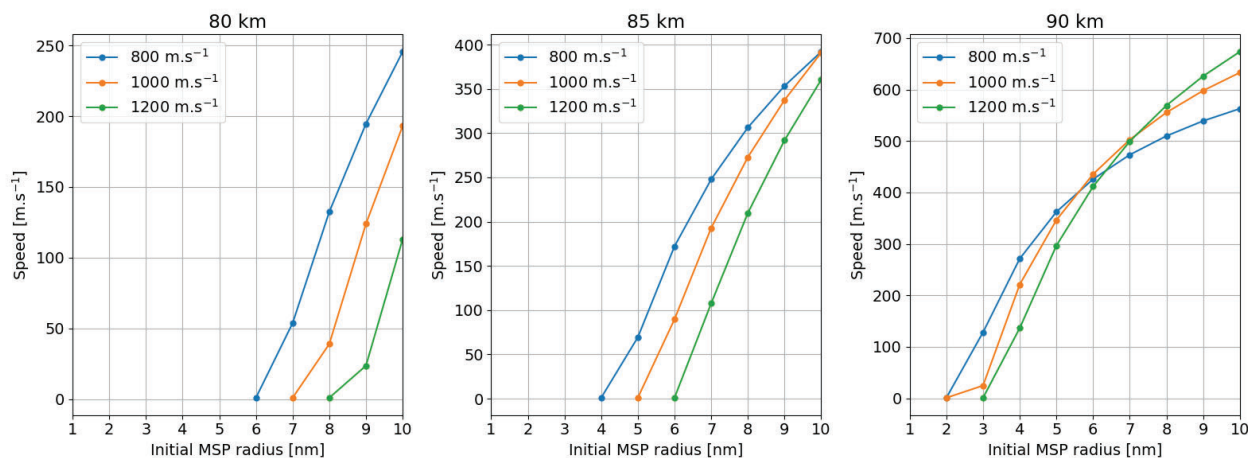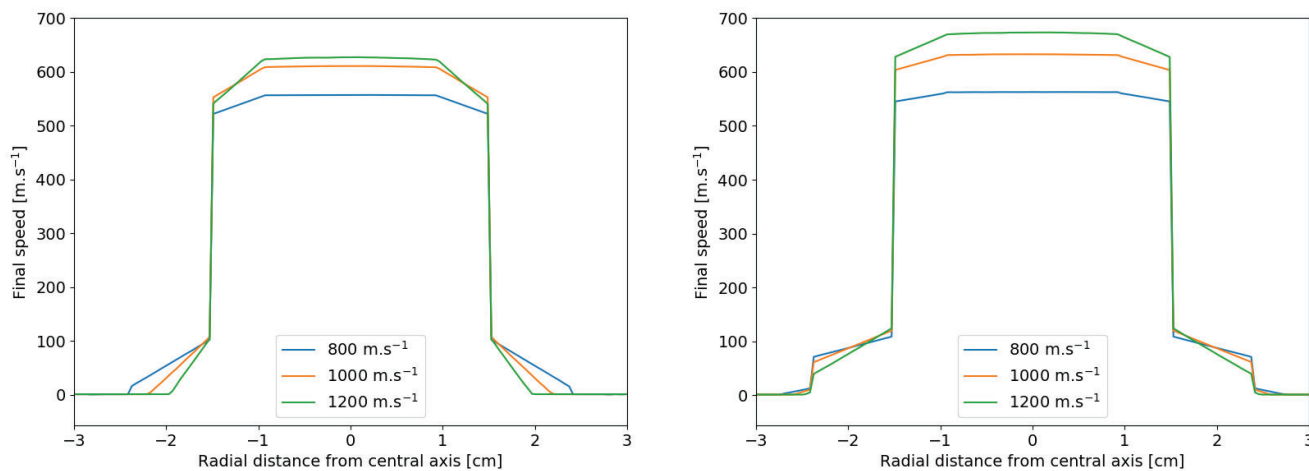
Figure 13. Final speed of MSP when they reach the collection area

(a) Radial profiles of the final speed of ice particles associated to an altitude of 82km and an initial radius of 20nm.

(b) Radial profiles of the final speed of MSP associated to an altitude of 85km and an initial radius of 10nm.

Figure 14. Profiles of the final speed of ice particles and MSP along the radial dimension for three different rocket speeds.

from binned height intervals between 80 and 90 km. In the same way, we estimate the number density of ice particles. We sum up the collected ice particles for the height interval 82 to 85 km because in the considered data this is where the vast majority of ice mass is accumulated.

The estimated amount of collected MSP material is listed the Table 3 for the directly collected MSP and for the MSP contained in the ice particles. The total collected mass ranges between 10^{15} amu and 10^{17} of refractory MSP. The mass per

Rocket velocity	$\left[\text{m s}^{-1}\right]$	800	1000	1200
Mass in MSP direct collection	10×10^{16} amu	12.62	8.341	5.915
Mass of MSP in collected ice particles	10×10^{16} amu	0.9620	1.001	1.042

Table 3. Estimates of the toal MSP mass collected as discuused in the text.

surface area at the collector is in the range of $10^{13}-10^{15}$ amu per mm^2. We note the uncertainties in the model assumptions and large variety of atmospheric conditions that influence the estimate. The listed values suggest that in spite of the limitations due to airflow detection, the amount of material directly impacting from MSP is larger than the material collected in the ice particles. We note that this is caused by us limiting the ice particles to those observed by optical methods. Since those large particles are less influenced by the airflow conditions the collected mass does not very much with the rocket velocity. The directly collected MSP are in majority of sizes larger than 5 nm and their total collected mass doubles from the 1200 m/s to the 800 m/s rocket velocity.

5 Conclusions

The proposed MESS design for collecting dust during rocket flight through a PMSE layer can return of the order of 10^{14} to 10^{15} amu of refractory MSP material assuming that the rocket samples a 0.5 - 4 km height interval of PMSE and that the collected ice particles contain a 3 percent volume fraction of refractory MSP. For particles that reach the collecting area, we find a range of impact energies between 10^{-3} eV and 10^6 eV. This is partly a result of the range of particle sizes, but impact energies also vary considerably for particles of the same size. The collected particles are primary particles and secondary particles that were affected by fragmentation at the funnel, both lose their ice component either during the collection or later during the campaign.

The collision process at the funnel induces an uncertainty. The dust temperatures increase in the instrument and we find that the temperature of the smallest fragments can possibly be higher than those that the collection reaches during the re-entry. It is also possible that some dust material will stick to the funnel and therefore will not reach the collector. The laboratory measurements that Tomsic et al. (2003) carried out with pure ice particles support our hypothesis that the dust particles will fragment at the funnel. We did not consider the cases that particles can stick at the funnel surface, nor did we consider charge effects. Dust particles can carry an initial charge and can also be charged during fragmentation. The inclusion of charged dust particles could result in an enhanced sticking to the walls and changes in the particle trajectory. In addition, the rocket payloads tend to become charged in their trajectory through the ionosphere. However, it has been shown that this charging in the mesosphere is small (Lai, 2011).

A further unknown is the orientation of the instrument relative to the airflow. Our estimates were made for a normal impact direction of particles to the instrument. In the case that the flux direction is tilted relative to the normal (angle of attack), which it most often is for sounding rockets, the impact angle from the surface normal is smaller for the particles impacting on the funnel. This has an influence on the fragmentation process. The airstream and hence dust flux are further modulated by coning

21

due to the rotation of the payload rotation axis. In the absence of a funnel, the direct flux of particles would be reduced because of the rocket tilt with respect to its direction of motion, which is less so the case with the funnel. In order to account for the angle-of-attack, the simulations would have to be expanded to 3D, including a 3D neutral gas flow, but this is out of the scope of this paper. Since an angle of attack can not be avoided, there will always be a fraction of particles hitting the side walls, i.e. the funnel.

In summary, the discussed design of a sample collector combined with a funnel increases the amount of collected dust mass by up to a factor of 7 because it has a larger sampling area. There is a cut-off for small particles that will not be collected. At 85 km, MESS will collect particles larger than roughly 4 nm radius. The cut-off for small particles is lower in the absence of a funnel, but the sampling area would be reduced. Dust collection with MESS should aim toward the higher altitude of PMSE. Our simulations suggest that for the same amount of dust in the atmosphere, a significantly higher amount of particles reach the collecting area at an altitude of 85 km in comparison to 80 km. With increasing rocket velocity, the amount of background gas in the instrument increases and so does the deceleration of particles in the instrument.

Code availability. The DS2V program can be found at http://www.gab.com.au/page4.html

Competing interests. The authors declare that they have no conflict of interest.

Appendix A: Calculation of the MSP fragments radii

According to the fragmentation modeling presented in Section 3.3, the mass conservation during the collision reads :

$$m_d = m_{1/2} + \sum_{f=1}^{n} m_f \tag{A1}$$

410 where $m_{1/2} = m_d/2$ corresponds to the mass of the large fragment that is supposed to be half of the mass of the incoming dust particle m_d and n the number of fragments constituted of MSP having a mass m_f. The composition of the dust particles gives :

$$m_d = \frac{4}{3}\pi \left(x_{MSP}\rho_{MSP} + x_{ice}\rho_{ice} \right) r_d^3 \tag{A2}$$

where $x_{MSP} = 3\%$ and $x_{ice} = 97\%$ respectively corresponds to the MSP and ice mass fraction of the dust particle. The small fragments are supposed to be small enough so that the ice they can contain sublimates immediately. This leads to :

415 $$\sum_{f=1}^{n} m_f = \frac{1}{2}x_{MSP}m_d \tag{A3}$$

according to the mass conservation and the dust particle composition. Assuming that all the fragments can be characterized by a radius r_f, one has by using Equation (A2) :

$$\sum_{f=1}^{n} r_f^3 = \bar{\rho} r_d^3 \tag{A4}$$

where it has been defined $\bar{\rho} = x_{MSP} \left(x_{MSP}\rho_{MSP} + x_{ice}\rho_{ice} \right)/2\rho_{MSP}$. By writing this equation in terms of the the radius distribu-
420 tion of the MSP fragments $\omega(r)$, it becomes :

$$\sum_{r=r_{min}}^{r=r_{max}} \omega(r)r^3 = \bar{\rho} r_d^3 \tag{A5}$$

where r_{min} and $r_{max} = \bar{\rho}^{1/3} r_d$ represent the radius of the smallest and largest MSP fragments respectively. The largest MSP fragment corresponds to the MSP fragment existing if only one is created. If the number of MSP fragments is large enough so that the radius distribution can be assumed as continuous over the fragments radius, we end up with :

425 $$\sum_{r=r_{min}}^{r=r_{max}} \omega(r)r^3 = \frac{\int_{r_{min}}^{r_{max}} \omega(r)r^3 \, dr}{\int_{r_{min}}^{r_{max}} r^3 \, dr} \tag{A6}$$

Finally, based on previous works focusing on fragmentation size distribution (Antonsen et al., 2020), the radius distribution can be assumed to scale as $\omega(r) \propto r^{-3}$. The integrals in the previous equation can be calculated analytically leading to :

$$\sum_{r=r_{min}}^{r=r_{max}} \omega(r)r^3 = 2\frac{r_{max}^2 r_{min}^2}{r_{max} + r_{min}} \tag{A7}$$

from which we defined :

430 $$r_{mean} = \left(2\frac{\bar{\rho}^{2/3} r_d^2 r_{min}^2}{\bar{\rho}^{1/3} r_d + r_{min}} \right)^{1/3} \tag{A8}$$

as the mean radius of the MSP fragments. The Figure A1 shows this mean radius as a function of the dust particle radius for the different and relevant values of r_{min}. It appears that $r_{mean} < 0.8$ nm for most the dust particles radii which means that the geometry of the MSP fragments has to be considered if one wants to track them.
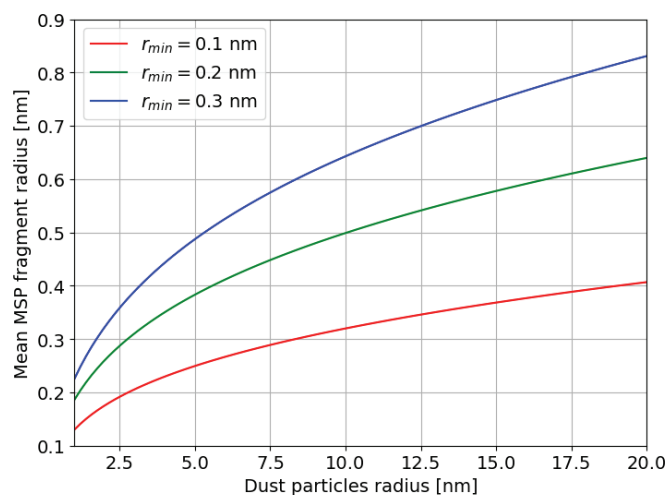
23

Figure A1. Mean MSP fragment radius as a function of the dust particle radius for three different value of r_{min}.

References

435 Antonsen, T. and Havnes, O.: On the detection of mesospheric meteoric smoke particles embedded in noctilucent cloud particles with rocket-borne dust probes, Review of Scientific Instruments, 86, 033 305, 2015.

Antonsen, T., Mann, I., Vaverka, J., Nouzak, L., and Fredriksen, Å.: A Comparison of Contact Charging and Impact Ionization in Low Velocity Impacts: Implications for Dust Detection in Space, Annales Geophysicae Discussions, pp. 1–26, 2020.

Baines, M., Williams, I., Asebiomo, A., and Agacy, R.: Resistance to the motion of a small sphere moving through a gas, Monthly Notices
440 of the Royal Astronomical Society, 130, 63–74, 1965.

Baumann, C., Rapp, M., Kero, A., and Enell, C.-F.: Meteor smoke influences on the D-region charge balance - review of recent in situ measurements and one-dimensional model results, Annales Geophysicae, 31, 2049–2062, https://doi.org/10.5194/angeo-31-2049-2013, https://angeo.copernicus.org/articles/31/2049/2013/, 2013.

Baumgarten, G., Fiedler, J., and Von Cossart, G.: The size of noctilucent cloud particles above ALOMAR (69N, 16E): Optical modeling and
445 method description, Advances in Space Research, 40, 772–784, 2007.

Baumgarten, G., Fiedler, J., and Rapp, M.: On microphysical processes of noctilucent clouds (NLC): observations and modeling of mean and width of the particle size-distribution, Atmospheric Chemistry and Physics, 10, 6661–6668, 2010.

Berger, U. and Lübken, F.-J.: Trends in mesospheric ice layers in the Northern Hemisphere during 1961–2013, Journal of Geophysical Research: Atmospheres, 120, 11–277, 2015.

450 Bird, G. A. and Brady, J.: Molecular gas dynamics and the direct simulation of gas flows, vol. 5, Clarendon press Oxford, 1994.

Chulaki, A.: MSIS-E-90 Atmosphere Model, https://ccmc.gsfc.nasa.gov/modelweb/models/msis_vitmo.php, 2020.

Evans, A.: The Dusty Universe, Ellis Horwood library of space science and space technology: Series in astronomy, Wiley, https://books.google.com/books?id=xQpJAAAACAAJ, 1994.

Farlow, N. H., Ferry, G. V., and Blanchard, M. B.: Examination of surfaces exposed to a noctilucent cloud, August 1, 1968, Journal of
455   Geophysical Research (1896-1977), 75, 6736–6750, 1970.

Havnes, O., Antonsen, T., Hartquist, T., Fredriksen, Å., and Plane, J.: The Tromsø programme of in situ and sample return studies of
mesospheric nanoparticles, Journal of Atmospheric and Solar-Terrestrial Physics, 127, 129–136, 2015.

Hedin, J., Giovane, F., Waldemarsson, T., Gumbel, J., Blum, J., Stroud, R. M., Marlin, L., Moser, J., Siskind, D. E., Jansson, K., et al.: The
MAGIC meteoric smoke particle sampler, Journal of Atmospheric and Solar-Terrestrial Physics, 118, 127–144, 2014.

460   Hervig, M. E., Deaver, L. E., Bardeen, C. G., Russell III, J. M., Bailey, S. M., and Gordley, L. L.: The content and composition of meteoric
smoke in mesospheric ice particles from SOFIE observations, Journal of Atmospheric and Solar-Terrestrial Physics, 84, 1–6, 2012.

Horányi, M., Gumbel, J., Witt, G., and Robertson, S.: Simulation of rocket-borne particle measurements in the mesosphere, Geophysical
Research Letters, 26, 1537–1540, 1999.

Kiliani, J., Baumgarten, G., Lübken, F.-J., and Berger, U.: Impact of particle shape on the morphology of noctilucent clouds, Atmospheric
465   Chemistry and Physics, 15, 12 897–12 907, 2015.

Kossacki, K. J. and Leliwa-Kopystynski, J.: Temperature dependence of the sublimation rate of water ice: Influence of impurities, Icarus,
233, 101–105, 2014.

Lai, S. T.: Spacecraft charging, American Institute of Aeronautics and Astronautics, 2011.

Lübken, F.-J., Hillert, W., Lehmacher, G., and Von Zahn, U.: Experiments revealing small impact of turbulence on the energy budget of the
470   mesosphere and lower thermosphere, Journal of Geophysical Research: Atmospheres, 98, 20 369–20 384, 1993.

Mann, I.: Meteors, in: Landolt-Börnstein - Group VI Astronomy and Astrophysics Volume 4B: Solar System, edited by Trümper, J., pp.
563–581, Springer-Verlag Berlin Heidelberg, 2009.

Megner, L., Rapp, M., and Gumbel, J.: Distribution of meteoric smoke–sensitivity to microphysical properties and atmospheric conditions,
Atmospheric Chemistry and Physics, 6, 4415–4426, 2006.

475 Plane, J. M., Feng, W., and Dawkins, E. C.: The mesosphere and metals: Chemistry and changes, Chemical reviews, 115, 4497–4541, 2015.

Podolak, M., Pollack, J. B., and Reynolds, R. T.: Interactions of planetesimals with protoplanetary atmospheres, Icarus, 73, 163–179, 1988.

Rapp, M. and Lübken, F.-J.: Polar mesosphere summer echoes (PMSE): Review of observations and current understanding, Atmospheric
Chemistry and Physics, 4, 2601–2633, 2004.

Rapp, M., Plane, J. M. C., Strelnikov, B., Stober, G., Ernst, S., Hedin, J., Friedrich, M., and Hoppe, U.-P.: In situ observations of meteor
480   smoke particles (MSP) during the Geminids 2010: constraints on MSP size, work function and composition, Annales Geophysicae, 30,
1661–1673, 2012.

Rizk, B., Hunten, D., and Engel, S.: Effects of size-dependent emissivity on maximum temperatures during micrometeorite entry, Journal of
Geophysical Research: Space Physics, 96, 1303–1314, 1991.

Skorov, Y. V. and Rickman, H.: A kinetic model of gas flow in a porous cometary mantle, Planetary and Space Science, 43, 1587–1594,
485   1995.

Smirnov, R., Pigarov, A. Y., Rosenberg, M., Krasheninnikov, S., and Mendis, D.: Modelling of dynamics and transport of carbon dust particles
in tokamaks, Plasma Physics and Controlled Fusion, 49, 347, 2007.

Strelnikov, B., Rapp, M., and Lübken, F.-J.: A new technique for the analysis of neutral air density fluctuations measured in situ in the middle
atmosphere, Geophysical Research letters, 30, 2003.

490 Tanaka, K. K., Mann, I., and Kimura, Y.: Formation of ice particles through nucleation in the mesosphere, Atmospheric Chemistry and
Physics, 22, 5639–5650, 2022.

Tomsic, A., Marković, N., and Pettersson, J. B.: Scattering of Ice particles from a graphite surface: A molecular dynamics simulation study, The Journal of Physical Chemistry B, 107, 10 576–10 582, 2003.